Preparation of Au-Doped Two-Phase TiO_2 Nanoparticles by One-Step Method as Photocatalytic Applications

Rasha Jameel Neama[1*], Firas Kamel Mohamad Alosfur[1], Khawla Jemeal Tahir[1], Noor Jawad Ridha[1], and Luma Majeed Ahmed[2]

[1]*Department of Physics, College of Science, University of Kerbala, Kerbala 56001, Iraq*

[2]*Department of Chemistry, College of Science, University of Kerbala, Kerbala 56001, Iraq*

* ***Corresponding author:***

email: rsha.j@s.uokerbala.edu.iq

Received: January 1, 2024
Accepted: March 2, 2024

DOI: 10.22146/ijc.92687

Abstract: *The synthesis of pure TiO_2 and X% Au/TiO_2 NPs was achieved via a sol-gel technique. The influence of Au concentration on structural, morphological, and optical features, as well as photocatalytic activity, was studied. XRD analysis revealed the presence of crystallized titanium consisting of anatase and rutile phases. The surface composition and electronic structure of TiO_2 and X% Au/TiO_2 catalysts were investigated using XPS analysis. Au/TiO_2 consists of Ti 2p, O 1s, and Au 4f regions from XPS analysis. FESEM and TEM were utilized to analyze the morphology of the samples. FTIR spectrum indicated the presence of OH, CH_2, and Ti–O–Ti groups in TiO_2 samples, with an additional peak at 2108.89 cm^{-1} indicating the presence of gold in X% Au/TiO_2 samples. The specific surface area increased from 33.36 m^2/g for pure TiO_2 to 51.62 m^2/g after the doping of 2.5% Au NPs. The incorporation of Au on the TiO_2 surface significantly influenced the optical properties in the 490 to 590 nm region, observed through the UV-vis absorption spectrum. The 2% Au/TiO_2 NPs exhibited higher catalytic activity than pure TiO_2, degrading methylene blue dye by 72.43% within 120 min.*

Keywords: *Au; methylene blue; photocatalysis; sol-gel; TiO_2; XPS*

■ INTRODUCTION

Dyes are used by a variety of businesses to color their products. Dyes are applied to substrates to provide permanent color that will not fade whether exposed to water, light, oxidizing chemicals, sweat, or microbiological attack [1]. Because of these benefits, dyes are widely utilized in various industries, including textile, food, rubber, printing, cosmetic, medicine, plastic, concrete, and paper industries [2-3]. These enterprises generate massive amounts of wastewater including carcinogenic and poisonous dyes, polluting water, and rendering it unsafe for human consumption [4].

Among these businesses, the textile industry is the most dye-consuming, using textile dyes, which are highly complex compounds with several structural groups. Methylene blue (MB), a highly consumed ingredient in the dye industry, is extensively used to color silk, wool, cotton, and paper [5-6]. Since 2010, articles on the breakdown of MB dye have steadily increased. Some literature reviews on MB removal using adsorption [7], bioremediation [8], and various noncatalytic combinations [9] as carbons.

Semiconductor photocatalysts were considered because of their excellent chemical and photochemical stability, super-hydrophilicity, low toxicity, long lifespan, and low cost to degrade organic contaminants in water. Many semiconductors have been used as photocatalysis materials, such as TiO_2, ZnO, CuO, and so on [10-13]. TiO_2 has been commonly utilized as a photocatalyst because it is inexpensive, non-toxic, and has high stability [14-15]. The highest photocatalytic effectiveness is achieved when two phases of TiO_2 (rutile and anatase) are combined [16].

Several studies have been carried out on TiO_2 to enhance the performance of photocatalyst activity, including doping with organic materials [17-18], transition metals [19-21], non-metals [22-23], and noble metals [24]. Noble metal nanoparticles (NPs) can behave

as active sites, capturing photogenerated electrons and lowering the recombination rate. Furthermore, due to their surface plasmon resonance (SPR) capabilities in the visible region, metal NPs can improve light usage [25-26]. Doping TiO_2 with a noble metal, such as gold (Au), was discovered to be a more effective approach to increasing photocatalytic activity by closing the energy gap. Au is an appropriate candidate since it is more stable and does not oxidize [27]. Several methods for attaching metal NPs to nanostructured semiconductors have been used, including deposition precipitation [28], photo deposition [29], chemical spray [30], and impregnation [31]. This study used a wet chemical approach to synthesize Au/TiO_2 NPs at room temperature and investigated their optical, photocatalytic, and structural capabilities. Sol-gel method was used for preparing catalysts like Au/TiO_2 NPs. The sol-gel process, in general, entails converting a system from a liquid sol phase to a solid gel phase. This approach provides a few advantages over conventional methods. For example, the active metal and the support can be produced in the same step in supported metal catalysis [32]. In this work, Au/TiO_2 was prepared employing the sol-gel method. The structural and optical characteristics of the prepared NPs were achieved. Finely the samples were examined as photocatalyst material for MB degradation.

■ EXPERIMENTAL SECTION

Materials

Titanium(IV) Isopropoxide (TTIP, $Ti(C_{12}H_{28}O_4)$, 97%, Sigma-Aldrich company), hydrogen tetrachloroaurate trihydrate ($HAuCl_4{\cdot}3H_2O$, 97%, Glentham), ethanol (C_2H_6O, 99.9%, J. T. Baker), hydrogen chloride (HCl, $HClO_3$, 36.5–38.0%, J. T. Baker), and deionized water (DI, H_2O, high degree of purity) which were used in the catalyst synthesize. In an aqueous solution, MB ($C_{16}H_{18}ClN_3S$, 99%, Merck Organics) was used as a target pollutant.

Instrumentation

To investigate the structural properties of the prepared samples, X-ray diffraction (XRD) Philips's type PW1730 with Cu K_α radiation source at a wavelength of 1.54056 Å with current 30 mA and voltage (40 kV) was used. Diffraction data were characterized at 2θ in the scanning range of 10–80° and step width of 0.02°. The X-ray Photoelectron Spectroscopy (XPS) BESTEC EA10 spectrometer assessed the sample's surface properties. CASAXPS software (Casa XPS Version 2.3.16 PR 1.6) was used to fit the spectra to a Shirley background. The morphology and particle size of the produced sample were studied using the transmission electron microscopy (TEM) Philips EM 208S microscope and field emission scanning electron microscopy (FESEM) TESCAN - (MIRA3, LMU) with an operating voltage of about 20 kV. Specific surface area (BET) BELSORP Mini II device was used to measure the surface area of the sample by subjecting it to N_2 adsorption at a temperature of 77 K. The samples' optical characteristics were investigated using a Shimadzu-UV-vis spectrophotometer (UV-1900i) at room temperature. Fourier-transform infrared (FTIR) 8400S Shimadzu studying overtones, combinations, or harmonic vibrations at the mid-infrared area 4000–400 cm^{-1} was employed to identify the functional group of X% Au/TiO_2 samples.

Procedure

Preparation of the gold solution

The $HAuCl_4{\cdot}3H_2O$ (1 g) was dissolved in HCl 1 M (8.2 mL) under vigorous stirring at room temperature. The solution of $HAuCl_4{\cdot}3H_2O$ was kept in the dark which was marked as solution A1.

Preparation of the Au/TiO2 NPs

Two solutions were prepared for the preparation of X% Au/TiO_2 NPs. Solution A2 which consisted of 10 mL of TTIP dissolved in 50 mL of absolute ethanol and stirred for 10 min until the solution turned from transparent to a milky color. Then, solution A1 was added dropwise in different ratios (0.5%, 1%, 1.5%, 2%, and 2.5%) of Au under stirring at 600 rpm to solution A2.

Solution B consisted of 50 mL ethanol, 10 mL water, and 1 mL concentrated HCl, respectively. After 30 min of continuous stirring of solution A1, the solution A2 was added. Afterward, the mixture was

transferred to a glass flask and left undisturbed for 48 h to allow the gel to form. Next, the samples were dried to evaporate unwanted materials. This involved placing the samples in an oven set at 75 °C for approximately 60 h. Finally, the obtained powder was manually ground using a mortar and pestle. Subsequently, the powder was annealed in an ambient atmosphere at 450 °C for 2 h. The degree of annealing was used based on previous studies [33].

Photocatalytic activity study

The influence of six different catalysts (TiO_2, X% Au/TiO_2) on the photocatalytic degradation of MB was investigated and studied. The examinations were carried out under similar conditions to compare the obtained results. The photodegradation properties of prepared samples were evaluated in the presence of UV-vis light to assess their ability to degrade MB dye. The degradation of MB dye was tracked by observing the gradual decline in the absorption peak at 664 nm in the UV-vis absorption spectra as the reaction time increased. This particular absorption peak corresponds to MB and is indicative of its concentration in the solution.

Initially, 15 mg of TiO_2 or X% Au/TiO_2 NPs as catalysts was added to a 100 mL MB with a concentration of 10 ppm. To disperse the solid catalyst particles, the suspension was subjected to sonication for 10 min before using UV light (Xenon lamp, 250 W, 365 nm wavelength). Achieve adsorption-desorption equilibrium of the dye MB on the TiO_2 or X% Au/TiO_2 catalysts surface, and to minimize any errors arising from elementary adsorption, the solution was then placed undisturbed in a dark room for at least 30 min. A preliminary sample, consisting of approximately 4 mL, was extracted from the solution after the dark adsorption phase to determine the concentration of the MB dye remaining in the solution, denoted as the primary concentration (C_o). The illumination process was then started, and the samples were collected every 20 min for a total of 120 min. Finally, the solution was subjected to centrifugation at 4500 rpm for 10 min to eliminate any suspended particulates, and the absorbance was determined using a UV-vis. spectrophotometer.

■ RESULTS AND DISCUSSION

XRD Analysis

XRD pattern exhibits distinct diffraction peaks corresponding to the crystallographic planes of polycrystalline Au and TiO_2 in anatase and rutile phases. The XRD spectrum of the prepared samples is shown in Fig. 1. Exhibited a peak at 2θ = 25.5°, 48.2°, 54.5°, 63.2°, and 69.2° which assigned to 101, 200, 105, 204, and 116, respectively, crystal lattice planes of TiO_2 in anatase phase (JCPDS card no. 002–0406). While peaks at 2θ = 27.8°, 36.3°, 39.4°, 41.4°, 44.4°, 56.9°, 64.3°, and 70.0° were assigned to 110, 101, 200, 111, 210, 220, 310, and 112, respectively, revealed the rutile phase of TiO_2 (JCPDS card no. 01-088–1173).

A peak at 2θ value of around 38.14° was observed revealing the existence of metallic Au which is assigned to 111 and this peak matches well with the face-centered cubic (FCC) Au NPs (JCPDS Card no. 004–0784). According to the standard, the appearance of this same peak in the pure TiO_2 as well as the Au metal has other peaks in the higher regions of 2θ that may overlap with the peaks of TiO_2 or may not have an obvious intensity due to its small amount [34].

The stronger peak results in the XRD test agree with the 110 plane appearing at 27.76° of the diffraction patterns, indicating the TiO_2 tetragonal rutile phase

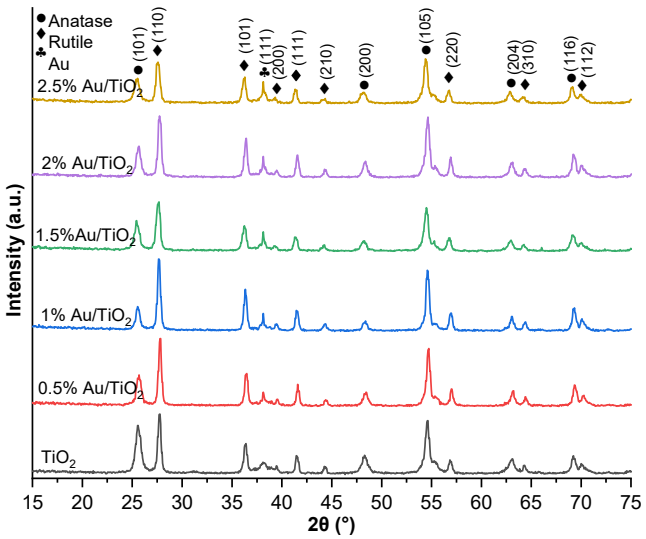

Fig 1. XRD patterns of TiO_2 and X% Au/TiO_2 NPs

formation. The Debye-Scherrer formula by used to determine the samples' average crystallite size [35-36]. The determination of the ratio of anatase to rutile phase can be achieved through the application of the Spurr's-Myers equation [37], utilizing the Origin software (version 2018). Eq. (1), derived from analyzing areas under the highest normalized peak intensities of a diffraction pattern, enables the calculation of the anatase and rutile phases;

$$\text{Rutile\%} = \frac{1}{1+0.8\left[\frac{I_A}{I_R}\right]} \quad (1)$$

where, I_R is the area under the highest normalized peak intensities of the rutile phase, and I_A is the area under the highest normalized peak intensities of the anatase phase. The results of the ratio of anatase to rutile, as well as the crystallite size for all samples, are presented in Table 1.

Only one peak was observed for gold at 2θ = 38.14°, and the rest of the peaks may be overlapping with titanium peaks in other areas. Therefore, it was observed that the average crystal dimensions of the gold-plated samples were relatively reduced compared to the pure sample. It is worth noting that this phenomenon may be ascribed to the imposition of lattice strain, thereby offering a plausible explanation for the observed reduction in crystallite size among the Au-doped specimens [38]. The highest anatase to rutile phase transformation occurred when 2.5% Au was used as the dopant (39.36% anatase and 60.63% rutile). Thus, it can be concluded that doping Au into the TiO_2 structure promotes the transition from the anatase to the rutile phase. Previous studies have shown that this transformation is influenced by factors such as the composition, grain size, impurities, nature and amount of dopant, and the heat treatment process [39].

Previous research has indicated that factors such as synthesis method, calcination temperature, and metal-doped can influence the crystal phase formation of TiO_2 [40]. It has been recently reported that the mixed phases of TiO_2 are useful for reducing the recombination of photogeneration electrons and holes that would raise the photocatalytic activity [41]. However, the rutile phase is also preferred for a synthesized TiO_2 structure because it could be used to improve the photocatalysis activity of TiO_2 [42].

XPS Analysis

Description of XPS for an illustrative of pure TiO_2 and X% Au/TiO_2 NPs regions Au 4f, Ti 2p, O 1s, and C 1s and related data. Fig. 2 shows the surface survey XPS

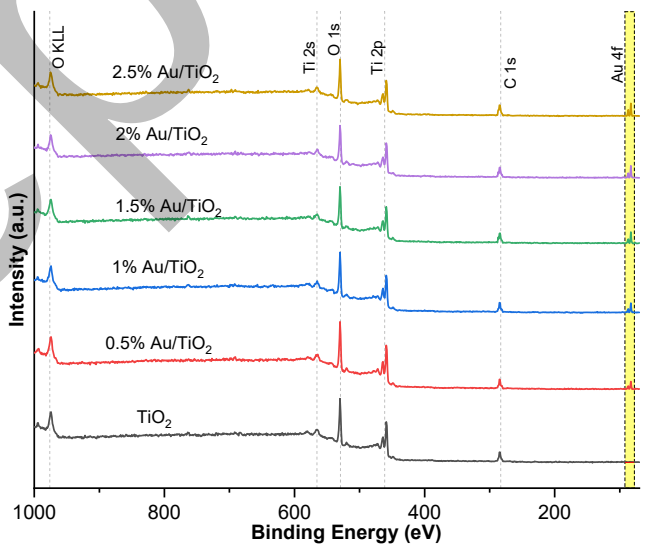

Fig 2. The XPS spectra of pure TiO_2 and X% Au/TiO_2 NPs

Table 1. The ratio of rutile phase and anatase and crystallite size of the samples

Sample	Phase ratio (%)		Crystallite size of TiO_2 (nm)	
	Anatase	Rutile	Anatase	Rutile
TiO_2	46.34	53.66	32.38	37.37
0.5% Au/TiO_2	44.85	55.15	32.39	35.50
1% Au/TiO_2	44.30	55.70	33.24	35.49
1.5% Au/TiO_2	41.49	58.51	28.96	28.65
2% Au/TiO_2	40.66	59.34	31.63	31.38
2.5% Au/TiO_2	39.36	60.64	33.97	26.37

spectra of pure TiO_2 and X% Au/TiO_2 NPs. The C 1s binding energy is caused by a thin coating of carbonaceous material produced on the surface of most samples exposed to air [43]. The survey spectra reveal two further peaks for X% Au/TiO_2 NPs in the region of 80–90 eV.

The Ti 2p region spectra of pure TiO_2 and X% Au/TiO_2 NPs are shown in Fig. 3(a). Ti (IV) $2p_{3/2}$ and $2p_{1/2}$ are the two main photoelectron peaks of pure TiO_2 at binding energies of 458.0 and 463.8 eV, respectively. For X% Au/TiO_2 NPs, it is discovered that the Ti $2p_{3/2}$ and $2p_{1/2}$ peaks have been moved to lower binding energies. The shift in binding energies can be attributed to the change in the surface chemistry of TiO_2 in the X% Au/TiO_2 NPs. This is because the Energy Fermi (E_f) of Au is known to be lower (−5.5 eV) than that of TiO_2 (−4.4 eV) [44,45]. This suggests intimate contact between TiO_2 and Au NPs, resulting in a change in electronic characteristics [46]. As a result, in the case of X% Au/TiO_2, electrons wander from TiO_2 to Au, making TiO_2 slightly positively charged. As a result, Ti 2p peaks at lower binding energy levels for the X% Au/TiO_2 NPs. The X% Au/TiO_2 sample's metallic state of Au NPs was indicated by the photoelectron peaks of Au (Fig. 3(b)), specifically Au $4f_{7/2}$ and $4f_{5/2}$, which were found to be located in the range of 82.02 to 89.35 eV for X% Au/TiO_2 samples.

Due to an electron transfer from TiO_2 to Au NPs. The binding energy of X% Au/TiO_2 was shown to be negatively shifted in the Au 4f signal, and this shift continued to decrease as the Au concentration increased, because Au NPs are dispersed on the TiO_2 surface, the electrons from the TiO_2 can transfer to the Au NPs, resulting in a change in the electronic structure of the around the Au NPs, leading to a negatively shifted binding energy in the Au 4f signal.

The potential cause of the negative energy shift is hypothesized to be the interaction of the Au particles with Ti. According to the literature, an initial state effect linked to electron transport from Ti^{3+} surface defect sites to Au can explain why the Au $4f_{7/2}$ peak shifted toward lower binding energy [44,47].

A marked shift in the binding energy is also observed for the O 1s of X% Au /TiO_2 NPs compared to that of pure TiO_2 NPs, as shown in Fig. 4. The lattice oxygen (LO) and surface-adsorbed oxygenated species (SO) are responsible for the high peak at 529.15 eV and the faint peak at 530.19 eV, respectively, in the O 1s feature of pure TiO_2 NPs (Fig. 4(a)). It is discovered that these two O 1s peaks have been moved to a higher binding energy, as shown in Fig. 4(b-f) [48]. The presence of LO and SO suggests the possibility of oxygen vacancies in the TiO_2 NPs. Oxygen vacancies can result in charge redistribution within the material, leading to a shift in the binding energy of the O 1s peaks towards higher energy. Table 2 displays the outcomes of the XPS analysis conducted on samples, encompassing both

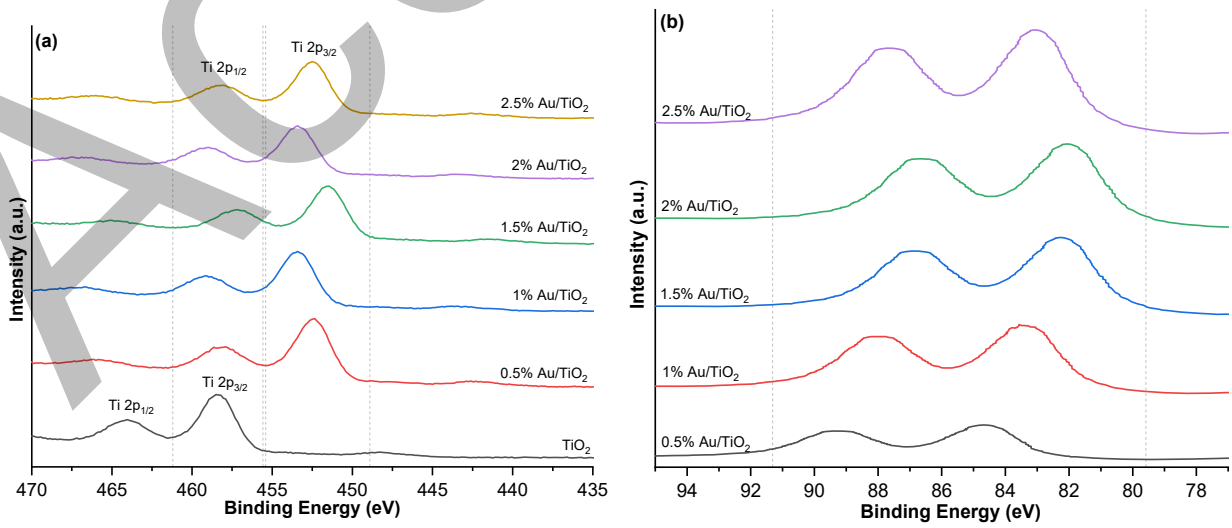

Fig 3. The surface survey XPS spectra of pure TiO_2 and X% Au/TiO_2 NPs for (a) Ti 2P and (b) Au 4f

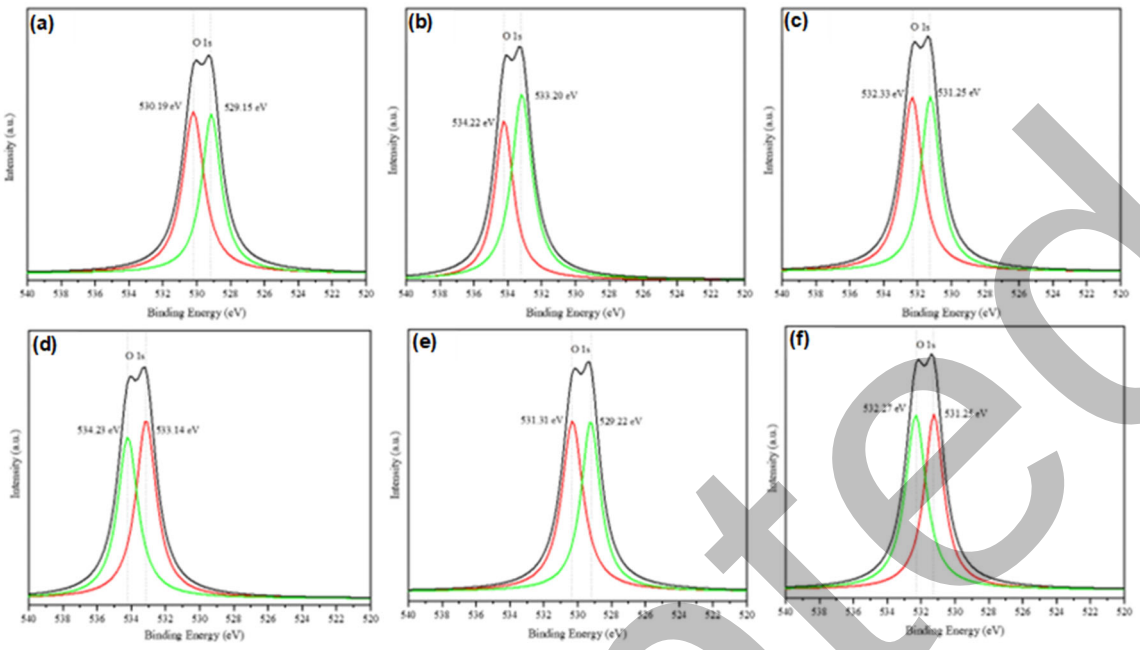

Fig 4. O 1s, XPS area spectra of (a) TiO_2, (b) 0.5% Au/TiO_2, (c) 1% Au/TiO_2, (d) 1.5% Au/TiO_2, (e) 2% Au/TiO_2, and (f) 2.5% Au/TiO_2

Table 2. The ratio of rutile phase and anatase and crystallite size of the samples

Sample	C 1s (%)	Ti $2p_{3/2}$ (%)	O 1s (%)	Au $4f_{7/2}$ (%)
TiO_2	9.30	24.64	66.06	--
0.5% Au/TiO_2	9.00	26.60	67.10	0.30
1% Au/TiO_2	8.20	29.84	61.16	0.80
1.5% Au/TiO_2	7.24	25.70	65.81	1.25
2% Au/TiO_2	7.71	24.42	65.52	1.45
2.5% Au/TiO_2	6.72	24.20	67.07	2.01

atomic ratios and the precise determination of peak positions.

TEM Analysis

TEM images were utilized to demonstrate the shape, particle size, and particle size distribution of pure TiO_2 and X% Au/TiO_2 NPs. Fig. 5 depicts the aggregation of particles consisting of either single particles or clusters of particles, the TiO_2 and X% Au/TiO_2 NPs had an uneven form of produced NPs in a TEM image. The morphology of TiO_2 remained same-like with the addition of Au, as illustrated in Fig. 5 where the Au NPs are evenly distributed over the surface of TiO_2.

The particle size and the distribution of TiO_2 and X% Au/TiO_2 samples are shown in the size distribution histogram (Fig. 6). The particle sizes observed were 31, 29, 28, 30, 28, and 29 nm for TiO_2, 0.5%, 1%, 1.5%, 2%, and 2.5% Au/TiO_2, respectively.

FESEM Analysis

FESEM was used to examine the morphology of the prepared samples, as Fig. 7 illustrates. The structure of the synthesized TiO_2 has agglomerated non-uniform spherical NPs, according to the results. The reason for the agglomeration is that TiO_2 is unstable in NPs form and will tend to clump together until it reaches a more stable state. The findings were in good agreement with previously published research [49]. Nevertheless, it was not evident that Au NPs were separate entities on the surface of Au/TiO_2 [50]. There were no discernible changes in the morphology of the TiO_2 and X% Au/TiO_2 samples.

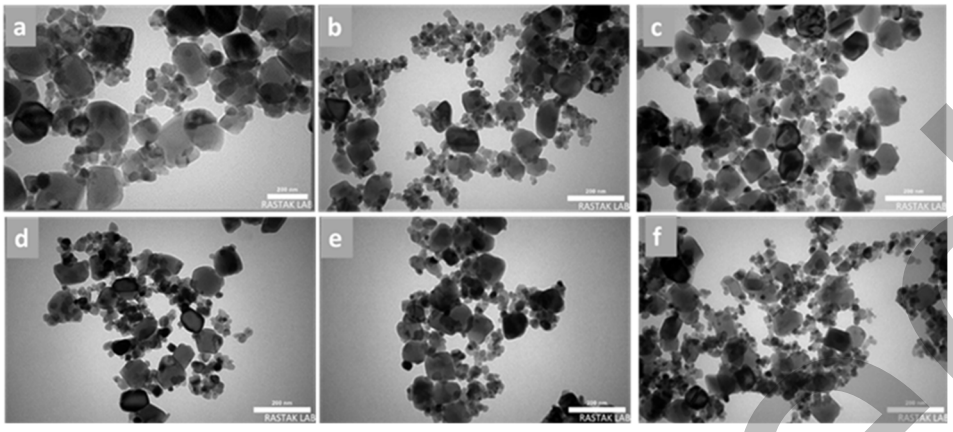

Fig 5. The TEM images of (a) TiO_2, (b) 0.5% Au/TiO_2, (c) 1% Au/TiO_2, (d) 1.5% Au/TiO_2, (e) 2% Au/TiO_2, and (f) 2.5% Au/TiO_2 samples

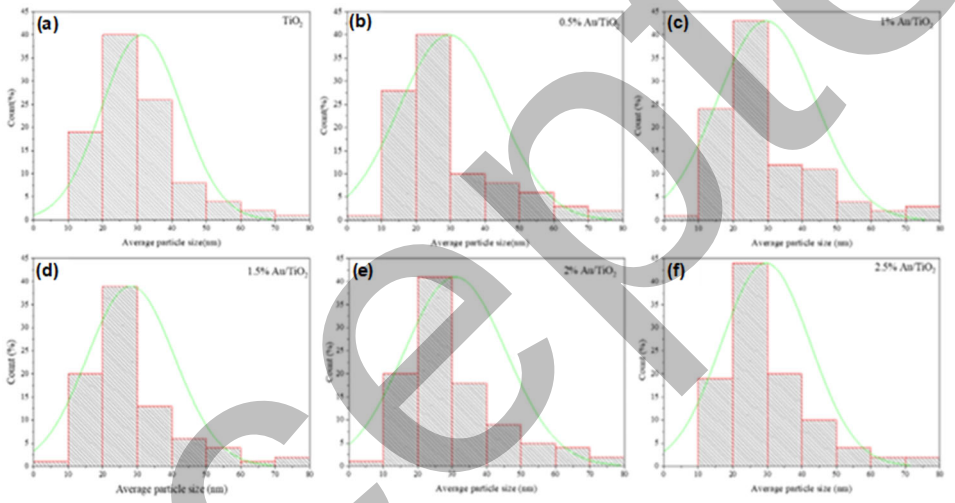

Fig 6. The size distribution histogram of (a) TiO_2, (b) 0.5% Au/TiO_2, (c) 1% Au/TiO_2, (d) 1.5% Au/TiO_2, (e) 2% Au/TiO_2, and (f) 2.5% Au/TiO_2 samples

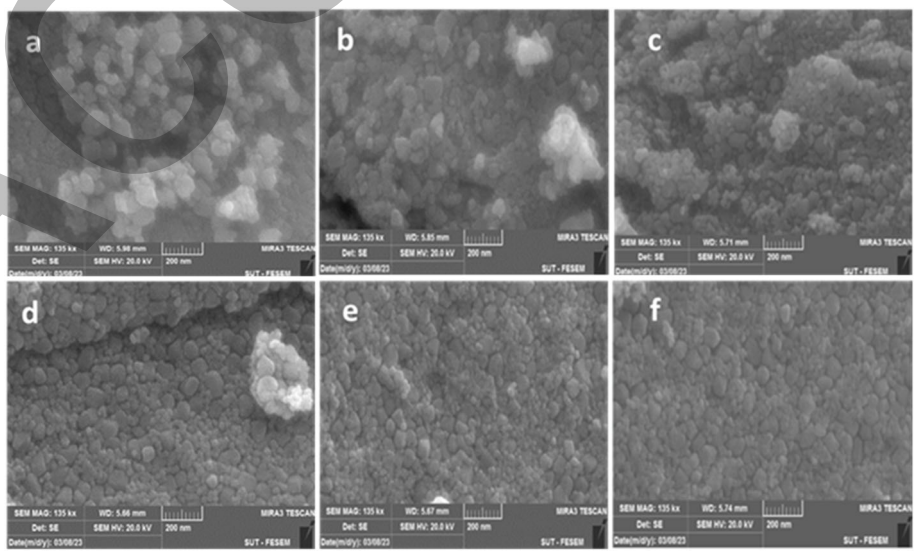

Fig 7. FE-SEM of (a) 0%, (b) 0.5%, (c) 1%, (d) 1.5%, (e) 2%, and (f) 2.5% Au/TiO_2 samples

The EDX mapping technique provides a comprehensive visualization of the elemental composition and spatial distribution of both TiO_2 and 2% Au/TiO_2 NPs, as shown in Fig. 8. Notably, the Au NPs exhibit a significantly uniform dispersion across the surface of the TiO_2 material. Usually, the weight percentage (wt.%) and atomic percentage (at%) of the surface elements of the sample are reported in the EDX analysis. The obtained data from the analysis confirmed the existence of Au metal on the surface of the catalyst as determined in Table 3.

Notably, the remaining samples exhibited slight contradictions between the observed percentage of Au within the sample structure and the expected value, as mentioned in Table 3. Discrepancies between expected and actual values for the proportion of Au within the sample structure can be caused by a variety of variables, including uncertainty in the compositions of the standards and inaccuracies in the different corrections that must be applied to the raw data [51].

BET Analysis

The surface area of the photocatalyst sample is an essential component that influences dye degradation activity [52]. Fig. 9 displays the N_2 adsorption-desorption curve of the TiO_2 and X% Au/TiO_2 NPs generated. The relative isotherms were type IV isotherms with an H1 hysteresis loop [53].

The occurrence of monolayer-multilayer adsorption on the inner surface becomes evident during the region i of the isotherms at low relative pressure (p/p_o). This is attributed to the transition from a fluid to

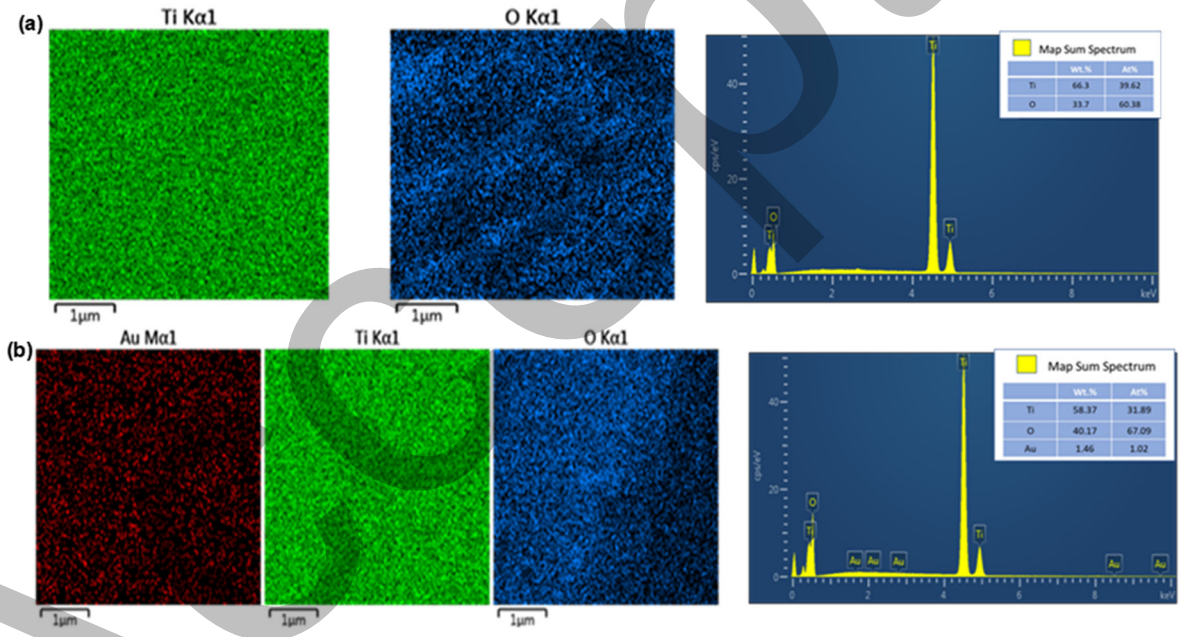

Fig 8. The EDX mapping of (a) TiO_2, and (b) 2% Au/TiO_2 samples

Table 3. The results of an EDX study of samples of TiO_2 and X% Au/TiO_2 NPs

Samples	wt.%			at.%		
	Au	Ti	O	Au	Ti	O
TiO_2	0.00	66.31	33.69	0.00	39.63	60.37
0.5% Au/TiO_2	0.32	59.66	40.02	0.21	33.37	66.42
1% Au/TiO_2	0.73	54.12	45.15	0.46	28.31	71.23
1.5% Au/TiO_2	1.11	60.02	38.87	0.09	34.31	65.60
2% Au/TiO_2	1.46	58.37	40.17	1.02	31.89	67.09
2.5% Au/TiO_2	2.01	63.17	34.82	1.12	36.42	62.46

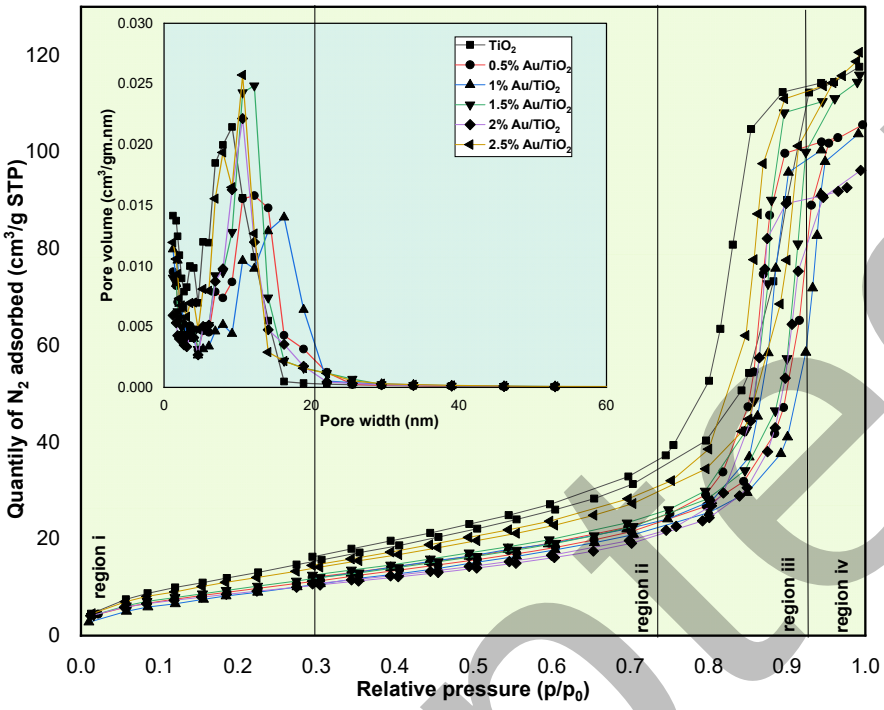

Fig 9. The pore diameter distribution and N_2 adsorption-desorption isotherms of the pure TiO_2 and X% Au/TiO_2 NPs at 77 K

Table 4. Surface area examination results of TiO_2 and X% Au/TiO_2, total pore volume, and average pore diameter

Catalyst	S_{BET} (m^2/g)	V_t (cm^3/g)	D_{BJH} (nm)
TiO_2	33.36	0.1481	17.75
0.5%Au/TiO_2	37.08	0.1625	17.52
1%Au/TiO_2	37.13	0.1602	17.25
1.5%Au/TiO_2	38.74	0.1772	16.29
2%Au/TiO_2	47.21	0.1846	15.63
2.5% Au/TiO_2	51.62	0.1816	14.07

*S_{BET}: surface area deduced from the isothermal analysis, V_t: pore volume overall, and D_{BJH}: the BJH adsorption technique used to calculate average pore diameter

a crystalline phase of the adsorbed N_2 [54]. Capillary condensation becomes noticeable at high p/p_o at regions ii and iii, as indicated by the pronounced increase in adsorption volume observed in the upper segment of isotherms once the pores have become saturated with N_2-liquid [55].

Table 4 provides a summary of the BET surface area, pore volume, and mean pore diameter of the samples examined. The BET surface area of TiO_2 was found to be a value close to that of X% Au/TiO_2 but showed a slight increase with higher Au loading. This suggests that the addition of Au had a limited impact on the BET surface area of TiO_2. In contrast, the introduction of Au into TiO_2 NPs resulted in a greater mesoporous volume compared to pure TiO_2. This increase can be attributed to the enhanced microporosity caused by Au doping which prevents TiO_2 NPs from clumping together. Additionally, the BJH pore diameter gradually decreased with the addition of Au, indicating controlled crystal growth in the X% Au/TiO_2 samples.

FTIR Spectra

The FTIR spectrum recorded from the TiO_2 and X% Au/TiO_2 samples is shown in Fig. 10. The absorption band observed at 3600–3400 cm^{-1} corresponds to the stretching vibration of the hydroxyl O–H group at 3735.21–3420.10 cm^{-1}. This result indicates the physical absorption of water, suggesting the presence of moisture in the samples [56]. The band at 2355.12 cm^{-1} indicates the stretching vibration of bonded and non-bonded O–H groups, resulting from the interaction of hydroxyl groups, and modes of the water molecules [57]. The enhanced intensity of the band at 2108.89 cm^{-1} suggests that most of the Au sites are covered by adsorbed oxygen [58]. This

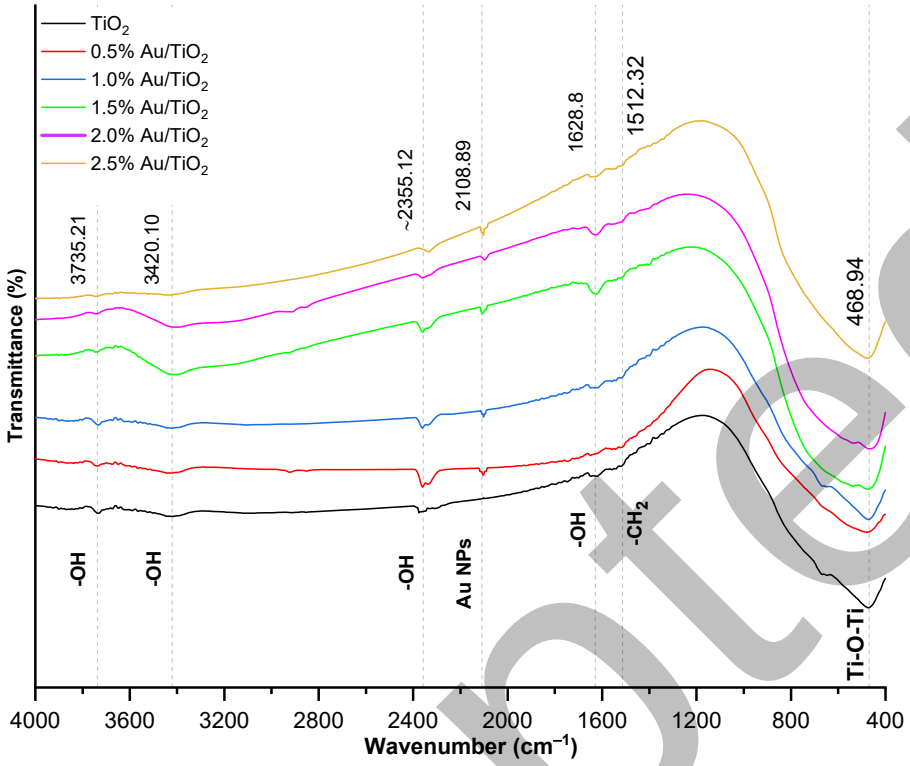

Fig 10. FTIR spectrum of the pure TiO_2 and X% Au/TiO_2 NPs

could be attributed to the presence of very small-sized Au NPs in the X% Au/TiO_2 samples, as previous research has shown that Au particles smaller than 2 nm remain oxidized [59-60]. The existence of this peak was not detected in the pure TiO_2 sample.

Furthermore, a weak band is observed at 1628.80 cm^{-1}, corresponding to O–H bending groups resulting from chemically absorbed water in the solution [61]. Another peak is detected at around 1512.32 cm^{-1}, characterized as the bending of CH_2 groups [62]. The peak at 468.94 cm^{-1} is observed, which is attributed to Ti–O–Ti stretching vibrations in the anatase and rutile phases. This indicates the broad absorbance of TiO_2 due to the bending vibration of Ti–O stretching, resulting in the formation of Ti–O–Ti bridge stretching [63].

UV-vis Analysis

The UV–vis absorption spectra of the TiO_2 and X% Au/TiO_2 NPs were recorded and are shown in Fig. 11(a). The TiO_2 showed no absorbance in the visible region because of the wide band gap (~3.2 eV). TiO_2 effectively absorbs light in the range of 275 to 405 nm and efficiently reflects light due to its high refractive index [64]. These dual effects, absorption, and reflection, significantly enhance TiO_2's protective capabilities against UV rays [65]. Conspicuous absorption within the wavelength range of 300–330 nm was discernible in all examined samples. Previous studies have substantiated the existence of a distinct peak at approximately 325 nm in pure TiO_2 [66]. Consequently, by introducing varying quantities of Au into the TiO_2 catalyst, the predictable modulation of the absorption wavelength has been demonstrated. A considerable increase in absorption was seen in X% Au/TiO_2 when the Au NPs were altered, maybe that's because the SPR effect of the Au NPs had a light-capturing effect [67]. Additionally, a distinct absorption peak emerged within the 490 to 590 nm range, aligning with the inherent absorption peak of Au. Increasing the Au content in the catalyst led to a proportional increase in light absorption. Fig. 11(b) presents the Tauc plot analysis used to calculate the band gap energy (E_g), specifically for a direct band gap semiconductor. The observed E_g of pure TiO_2 is 3.24 eV, which aligns well with the theoretical value. However, as

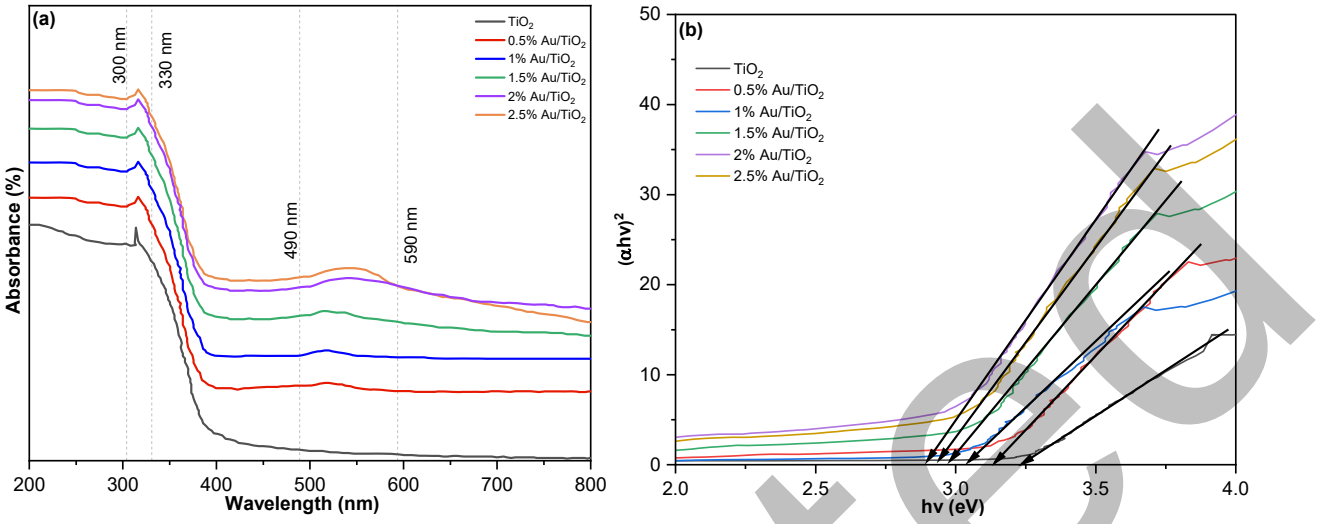

Fig 11. TiO_2 and X% Au/TiO_2 samples for (a) UV-vis absorption spectrum and (b) band gap energy

the amount of Au loading increases, there appears to be a decreasing trend in the E_g value. This is evident from the observed values of 3.14, 3.02, 2.98, 2.90, and 2.94 eV for the 0.5%, 1%, 1.5%, 2%, and 2.5% Au/TiO_2 samples, respectively. The decrease in E_g value is a result of the properties of free electrons in the conduction band (CB), indicating structural changes in the TiO_2 matrix upon loading of Au NPs onto TiO_2. This leads to the creation of a metal-semiconductor Schottky junction between Au and TiO_2 [68]. May be explained that when the content of Au was less than its optimal ratio, the gold impurity energy level would be the separation center. On the contrary, when the content of gold/gold ion was more than its optimal ratio, the gold impurity energy level would be a recombination center, which in turn makes the energy gap decrease.

MB Degradation

Initially, the influence of the amount of adsorbent on the photocatalytic degradation of MB dye was investigated using TiO_2. To determine the optimal dosage of the catalyst, various quantities of the TiO_2 catalyst were measured and subsequently evaluated for their photocatalytic efficacy under the same conditions. Thus, 5, 10, 15, 20, and 25 mg of adsorbent were employed. Subsequently, each of these catalyst doses underwent photocatalytic testing using identical operating conditions, including a concentration of MB dye at 10 ppm, a solution volume of 100 mL, and exposure to UV light irradiation for 120 min. The remaining concentration of MB dye in the supernatant was quantified by measuring its absorbance using a UV-vis spectrophotometer.

The results presented in Fig. 12 illustrate that the highest degradation efficiency for TiO_2 was observed at a dose of 15 mg, yielding a degradation percentage of 68.62%. Following this, doses of 5, 10, 15, 20, and 25 mg resulted in degradation percentages of 36.22, 57.41, 68.62, 48.78, and 47.27%, respectively, after 120 min of light irradiation. It was found that 15 mg TiO_2 shows higher activity in reaction and dye decomposition than 20 and 25 mg TiO_2. This can be attributed to that 15 mg

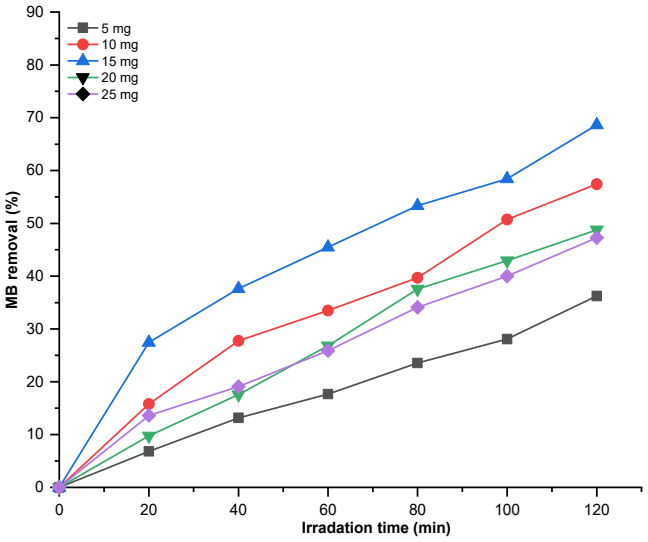

Fig 12. Effect of amount of TiO_2 on the degradation of MB dye at 120 min UV light irradiation

TiO_2 has the highest content of surface hydroxyl groups in contrast to the 20 and 25 mg samples which can be observed. On the other hand, when the amount of catalyst is increased more than the ideal amount, it leads to the solution becoming turbid and not transmitting to light, meaning its absorption of light decreases and the reaction is not completed.

Fig. 13 shows the time-dependent UV-vis spectra of MB in the presence of the synthesized 15 mg of pure TiO_2, 0.5%, 1%, 1.5%, 2%, and 2.5% Au/TiO_2 NPs under UV light irradiation. The results showed that as the time increased, the absorption decreased for all samples. The sample 2% Au/TiO_2 had the highest reduction in absorption. The time of irradiation increased, and the interaction of the dye molecule increased with the surface of the photocatalyst. Therefore, the photodegradation efficiency of the photocatalyst was increased [69-70].

The photocatalytic reaction rate is significantly influenced by the level of Au loading on the surface of TiO_2. To determine the most effective Au loading for this particular reaction, the photocatalytic degradation of MB under UV light irradiation was performed using Au/TiO_2 with varying amounts of Au for 0.5%, 1%, 1.5%, 2%, and 2.5%. The results showed that the photocatalyst with a 2% Au content exhibited the highest activity. The superior photocatalytic performance observed in the composite with 2% Au loading can be attributed to both enhanced light absorption and the strongest SPR effect [71]. While pure TiO_2 had the lowest reduction after 120 min of UV light exposure.

Fig. 14 illustrates the observed degradation rates of MB under various concentrations of X% Au/TiO_2 catalysts. Among the tested catalysts, the 2% Au/TiO_2 exhibited the highest degradation rate, reaching 79.88%. This was closely followed by the 1.5% Au/TiO_2 catalyst at 75.40%. Additionally, the 1%, 2.5%, 0.5% Au/TiO_2, and TiO_2 catalysts achieved degradation rates of 74.10, 73.23, 70.60, and 68.62%, respectively, after 120 min of light irradiation.

The reason for the reduced activity at high levels of Au can be explained by the fact that there is a limited number of sites on which both the metal and support are necessary for the reaction to take place [72]. Additionally, a high amount of Au can create a shadowing effect, which prevents the photocatalyst NPs from absorbing light [73]. A summary list of studies on

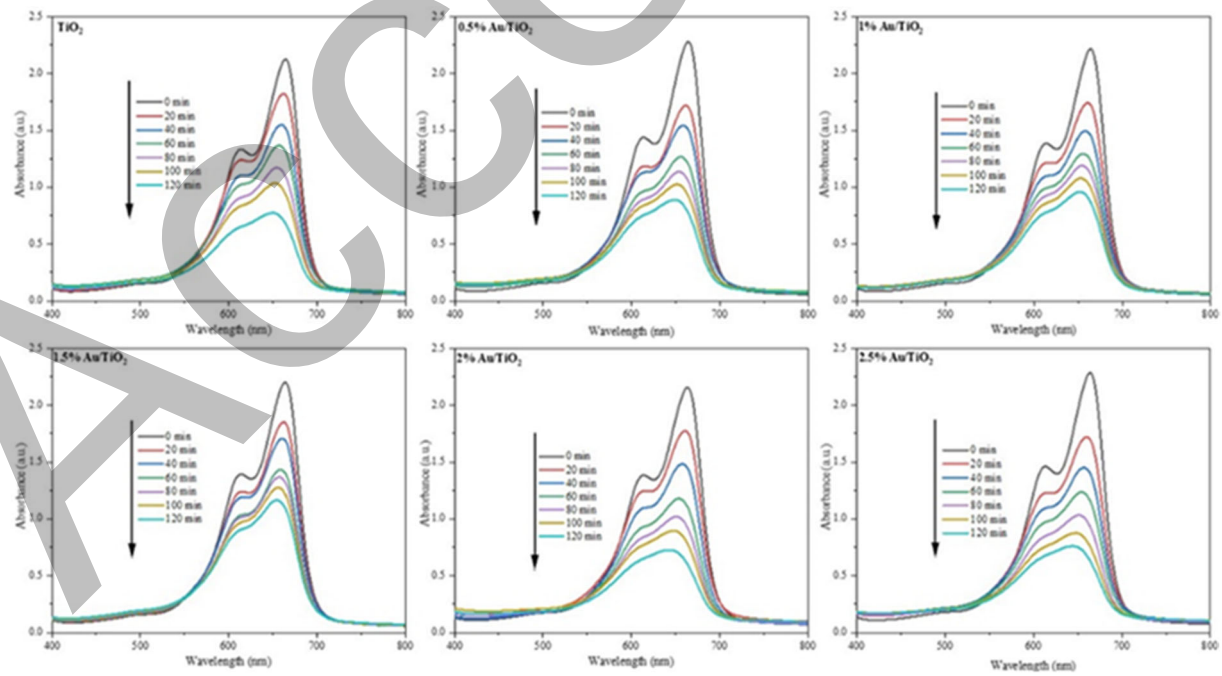

Fig 13. UV–vis spectra of MB degradation with initial concentration = 10 ppm, catalysts dose = 15 mg of TiO_2, X% Au/TiO_2, versus irradiation time for MB degradation

Table 5. List of recently investigated photocatalytic activity of TiO_2 and X% Au/TiO_2 for MB degradation under UV-vis irradiation studied by researchers

Catalyst	Rate of degradation (%)	Preparation method	Irradiation time (min)	Catalyst dose (mg)	[MB] (ppm)	Ref.
TiO_2	68.62	Sol-gel	120	15	10	This study
Au/TiO_2	79.88					
TiO_2	45.00	Sol-gel	80	25	10	[74]
Au/TiO_2	73.00					
TiO_2	50.00	Hydrothermal	120	-	10	[75]
Au/TiO_2	66.00					
TiO_2	50.00	Flame spray pyrolysis	200	6	20	[76]
Au/TiO_2	60.00					
TiO_2	92.00	Sol-gel	240	50	3	[77]
Au/TiO_2	96.48					
Au/TiO_2	93.90	Sol-gel	240	100	15	[78]

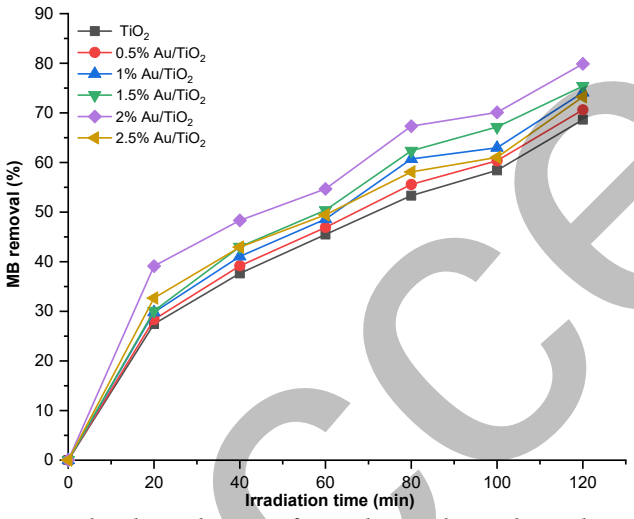

Fig 14. The degradation of MB dye with catalysts dose = 15 mg of TiO_2, and X% Au/TiO_2 at 120 min UV light irradiation

the photodegradation of MB by different photocatalytic nanocatalysts prepared by different physical and chemical methods is listed in Table 5.

■ CONCLUSION

A novel composite photocatalyst, Au-doped TiO_2, was effectively produced using the sol-gel process. Under both UV light irradiation conditions, the as-prepared photocatalyst exhibits more photocatalytic activity than pure TiO_2. The XRD results confirmed the Au and TiO_2 structures (rutile and anatase phases), the average crystallite size of the prepared TiO_2 NPs was 28–37 nm for the anatase and rutile phases. Through XPS, the surface components are revealed, which are Au 4f, Ti 2p, and O 1s regions. FESEM and TEM were utilized to analyze the morphology of the samples, and the results show spherical shapes. The FTIR spectrum indicated the presence of OH, CH_2, and Ti–O–Ti groups in TiO_2 samples, with an additional peak at 2108.89 cm^{-1} indicating the presence of gold in X% Au/TiO_2 samples. The BET surface measurement reveals that the surface area increases from 33.36 m^2/g for pure TiO_2 to 51.62 m^2/g for 2.5% Au/TiO_2. The UV-vis analysis result demonstrated that the as-synthesized X% Au/TiO_2 nanostructures were strongly absorbing at both UV and visible regions, i.e., 200–380 and 650 nm, respectively. The strong absorption at the UV region is believed to be due to the presence of a TiO_2 band gap, whereas the SPR phenomenon of Au NPs renders a strong absorption visible region. In the photocatalytic investigation, it was discovered that under identical reaction circumstances, 2% Au/TiO_2 was a superior photocatalyst to others. Doping TiO_2 samples with Au NPs is considered a promising work for purifying water from organic dyes.

■ ACKNOWLEDGMENTS

The authors acknowledge the College of Science at the University of Kerbala for the support.

■ CONFLICT OF INTEREST

There are no pertinent financial or non-financial interests that the authors need to disclose.

■ AUTHOR CONTRIBUTIONS

All of the writers influenced the idea and design of the study. Rasha Jameel Neama, Firas Kamel Mohamad Alosfur, Khawla Jemeal Tahir, Noor Jawad Ridha, and Luma Majeed Ahmed handled the material preparation, data gathering, and analysis. All contributors provided feedback on earlier drafts of the work, with Rasha Jameel Neama penning the original draft. The completed work was read and approved by all writers.

■ REFERENCES

[1] Khan, I., Khan, I., Usman, M., Imran, M., and Saeed, K., 2020, Nanoclay-mediated photocatalytic activity enhancement of copper oxide nanoparticles for enhanced methyl orange photodegradation, *J. Mater. Sci.: Mater. Electron.*, 31 (11), 8971–8985.

[2] Ahmad, A., Mohd-Setapar, S.H., Chuong, C.S., Khatoon, A., Wani, W.A., Kumar, R., and Rafatullah, M., 2015, Recent advances in new generation dye removal technologies: Novel search for approaches to reprocess wastewater, *RSC Adv.*, 5 (39), 30801–30818.

[3] Alencar, L.V.T.D., Passos, L.M.S., Soares, C.M.F., Lima, A.S., and Souza, R.L., 2020, Efficiency method for methylene blue recovery using aqueous two-phase systems based on cholinium-ionic liquids, *Curr. Trends Fashion Technol. Text. Eng.*, 6 (1), 13–20.

[4] Pandey, S., Do, J.Y., Kim, J., and Kang, M., 2020, Fast and highly efficient removal of dye from aqueous solution using natural locust bean gum-based hydrogels as adsorbent, *Int. J. Biol. Macromol.*, 143, 60–75.

[5] Derakhshan, Z., Baghapour, M.A., Ranjbar, M., and Faramarzian, M., 2013, Adsorption of methylene blue dye from aqueous solutions by modified pumice stone: Kinetics and equilibrium studies, *J. Health Scope*, 2 (3), 136–144.

[6] Fong, W.M., Affam, A.C., and Chung, W.C., 2020, Synthesis of Ag/Fe/CAC for colour and COD removal from methylene blue dye wastewater, *Int. J. Environ. Sci. Technol.*, 17 (7), 3485–3494.

[7] Santoso, E., Ediati, R., Kusumawati, Y., Bahruji, H., Sulistiono, D.O., and Prasetyoko, D., 2020, Review on recent advances of carbon-based adsorbent for methylene blue removal from wastewater, *Mater. Today Chem.*, 16, 100233.

[8] Zamel, D., and Khan, A.U., 2021, Bacterial immobilization on cellulose acetate-based nanofibers for methylene blue removal from wastewater: Mini-review, *Inorg. Chem. Commun.*, 131, 108766.

[9] Gan, J., Megonnell, N.E., and Yates, S.R., 2001, Adsorption and catalytic decomposition of methyl bromide and methyl iodide on activated carbons, *Atmos. Environ.*, 35 (5), 941–947.

[10] Raizada, P., Sudhaik, A., Patial, S., Hasija, V., Parwaz Khan, A.A., Singh, P., Gautam, S., Kaur, M., and Nguyen, V.H., 2020, Engineering nanostructures of CuO-based photocatalysts for water treatment: Current progress and future challenges, *Arabian J. Chem.*, 13 (11), 8424–8457.

[11] Schneider, J., Matsuoka, M., Takeuchi, M., Zhang, J., Horiuchi, Y., Anpo, M., and Bahnemann, D.W., 2014, Understanding TiO_2 photocatalysis: mechanisms and materials, *Chem. Rev.*, 114 (19), 9919–9986.

[12] Qi, K., Cheng, B., Yu, J., and Ho, W., 2017, Review on the improvement of the photocatalytic and antibacterial activities of ZnO, *J. Alloys Compd.*, 727, 792–820.

[13] Taufique, M.F.N., Haque, A., Karnati, P., and Ghosh, K., 2018, ZnO–CuO nanocomposites with improved photocatalytic activity for environmental and energy applications, *J. Electron. Mater.*, 47 (11), 6731–6745.

[14] Kunarti, E.S., Kartini, I., Syoufian, A., and Widyandari, K.M., 2018, Synthesis and

photoactivity of Fe_3O_4/TiO_2-Co as a magnetically separable visible light responsive photocatalyst, *Indones. J. Chem.*, 18 (3), 403–410.

[15] Manurung, P., Situmeang, R., Ginting, E., and Pardede, I., 2015, Synthesis and characterization of titania-rice husk silica composites as photocatalyst, *Indones. J. Chem.*, 15 (1), 36–42.

[16] Luo, Z., Poyraz, A.S., Kuo, C.H., Miao, R., Meng, Y., Chen, S.Y., Jiang, T., Wenos, C., and Suib, S.L., 2015, Crystalline mixed phase (anatase/rutile) mesoporous titanium dioxides for visible light photocatalytic activity, *Chem. Mater.*, 27 (1), 6–17.

[17] Khairy, M., and Zakaria, W., 2014, Effect of metal-doping of TiO_2 nanoparticles on their photocatalytic activities toward removal of organic dyes, *Egypt. J. Pet.*, 23 (4), 419–426.

[18] Valero-Romero, M.J., Santaclara, J.G., Oar-Arteta, L., van Koppen, L., Osadchii, D.Y., Gascon, J., and Kapteijn, F., 2019, Photocatalytic properties of TiO_2 and Fe-doped TiO_2 prepared by metal organic framework-mediated synthesis, *Chem. Eng. J.*, 360, 75–88.

[19] Song, K., Han, X., and Shao, G., 2013, Electronic properties of rutile TiO_2 doped with 4*d* transition metals: First-principles study, *J. Alloys Compd.*, 551, 118–124.

[20] Zhang, J., Fu, D., Wang, S., Hao, R., and Xie, Y., 2019, Photocatalytic removal of chromium (VI) and sulfite using transition metal (Cu, Fe, Zn) doped TiO_2 driven by visible light: Feasibility, mechanism and kinetics, *J. Ind. Eng. Chem.*, 80, 23–32.

[21] Widiyandari, H., Nashir, M., Parasdila, H., Almas, K.F., and Suryana, R., 2023, Ag-TiO_2 for efficient methylene blue photodegradation under visible light irradiation, *Bull. Chem. React. Eng. Catal.*, 18 (4), 593–603.

[22] Basavarajappa, P.S., Patil, S.B., Ganganagappa, N., Reddy, K.R., Raghu, A.V., and Reddy, C.V., 2020, Recent progress in metal-doped TiO_2, non-metal doped/codoped TiO_2 and TiO_2 nanostructured hybrids for enhanced photocatalysis, *Int. J. Hydrogen Energy*, 45 (13), 7764–7778.

[23] Di Valentin, C., and Pacchioni, G., 2013, Trends in non-metal doping of anatase TiO_2: B, C, N and F, *Catal. Today*, 206, 12–18.

[24] Sultana, M., Mondal, A., Islam, S., Khatun, M.A., Rahman, M.H., Chakraborty, A.K., Rahman, M.S., Rahman, M.M., and Nur, A.S.M., 2023, Strategic development of metal doped TiO_2 photocatalysts for enhanced dye degradation activity under UV–vis irradiation: A review, *Curr. Res. Green Sustainable Chem.*, 7, 100383.

[25] Tsukamoto, D., Shiraishi, Y., Sugano, Y., Ichikawa, S., Tanaka, S., and Hirai, T., 2012, Gold nanoparticles located at the interface of anatase/rutile TiO_2 particles as active plasmonic photocatalysts for aerobic oxidation, *J. Am. Chem. Soc.*, 134 (14), 6309–6315.

[26] Priebe, J.B., Radnik, J., Lennox, A.J.J., Pohl, M.M., Karnahl, M., Hollmann, D., Grabow, K., Bentrup, U., Junge, H., Beller, M., and Brückner, A., 2015, Solar hydrogen production by plasmonic Au–TiO_2 catalysts: Impact of synthesis protocol and TiO_2 phase on charge transfer efficiency and H_2 evolution rates, *ACS Catal.*, 5 (4), 2137–2148.

[27] Hurum, D.C., Agrios, A.G., Gray, K.A., Rajh, T., and Thurnauer, M.C., 2003, Explaining the enhanced photocatalytic activity of Degussa P25 mixed-phase TiO_2 using EPR, *J. Phys. Chem. B*, 107 (19), 4545–4549.

[28] Bumajdad, A., Madkour, M., Abdel-Moneam, Y., and El-Kemary, M., 2014, Nanostructured mesoporous Au/TiO_2 for photocatalytic degradation of a textile dye: The effect of size similarity of the deposited Au with that of TiO_2 pores, *J. Mater. Sci.*, 49 (4), 1743–1754.

[29] Veziroglu, S., Obermann, A.L., Ullrich, M., Hussain, M., Kamp, M., Kienle, L., Leißner, T., Rubahn, H.G., Polonskyi, O., Strunskus, T., Fiutowski, J., Es-Souni, M., Adam, J., Faupel, F., and Aktas, O.C., 2020, Photodeposition of Au nanoclusters for enhanced photocatalytic dye degradation over TiO_2 thin film, *ACS Appl. Mater. Interfaces*, 12 (13), 14983–14992.

[30] Oja Acik, I., Oyekoya, N.G., Mere, A., Loot, A., Dolgov, L., Mikli, V., Krunks, M., and Sildos, I., 2015, Plasmonic TiO_2: Au composite layers deposited *in situ* by chemical spray pyrolysis, *Surf. Coat. Technol.*, 271, 27–31.

[31] Rodríguez-Martínez, C., García-Domínguez, Á.E., Guerrero-Robles, F., Saavedra-Díaz, R.O., Torres-Torres, G., Felipe, C., Ojeda-López, R., Silahua-Pavón, A., and Cervantes-Uribe, A., 2020, Synthesis of supported metal nanoparticles (Au/TiO_2) by the suspension impregnation method, *J. Compos. Sci.*, 4 (3), 89.

[32] van Deelen, T.W., Hernández Mejía, C., and de Jong, K.P., 2019, Control of metal-support interactions in heterogeneous catalysts to enhance activity and selectivity, *Nat. Catal.*, 2 (11), 955–970.

[33] Du, M., Huang, J., Sun, D., Wang, D., and Li, Q., 2018, High catalytic stability for CO oxidation over Au/TiO_2 catalysts by *Cinnamomum camphora* leaf extract, *Ind. Eng. Chem. Res.*, 57 (44), 14910–14914.

[34] Yu, J., Yue, L., Liu, S., Huang, B., and Zhang, X., 2009, Hydrothermal preparation and photocatalytic activity of mesoporous Au–TiO_2 nanocomposite microspheres, *J. Colloid Interface Sci.*, 334 (1), 58–64.

[35] Patel, S.K.S., Jena, P., and Gajbhiye, N.S., 2019, Structural and room-temperature ferromagnetic properties of pure and Ni-doped TiO_2 nanotubes, *Mater. Today: Proc.*, 15, 388–393.

[36] Mustapha, S., Tijani, J.O., Ndamitso, M.M., Abdulkareem, A.S., Shuaib, D.T., Amigun, A.T., and Abubakar, H.L., 2021, Facile synthesis and characterization of TiO_2 nanoparticles: X-ray peak profile analysis using Williamson–Hall and Debye–Scherrer methods, *Int. Nano Lett.*, 11 (3), 241–261.

[37] Nkele, A.C., Chime, U.K., Asogwa, L., Nwanya, A.C., Nwankwo, U., Ukoba, K., Jen, T.C., Maaza, M., and Ezema, F.I., 2020, A study on titanium dioxide nanoparticles synthesized from titanium isopropoxide under SILAR-induced gel method: Transition from anatase to rutile structure, *Inorg. Chem. Commun.*, 112, 107705.

[38] Ibrahim, N.S., Leaw, W.L., Mohamad, D., Alias, S.H., and Nur, H., 2020, A critical review of metal-doped TiO_2 and its structure–physical properties–photocatalytic activity relationship in hydrogen production, *Int. J. Hydrogen Energy*, 45 (53), 28553–28565.

[39] Loan, T.T., Huong, V.H., Huyen, N.T., Van Quyet, L., Bang, N.A., and Long, N.N., 2021, Anatase to rutile phase transformation of iron-doped titanium dioxide nanoparticles: The role of iron content, *Opt. Mater.*, 111, 110651.

[40] Kim, M.G., Kang, J.M., Lee, J.E., Kim, K.S., Kim, K.H., Cho, M., and Lee, S.G., 2021, Effects of calcination temperature on the phase composition, photocatalytic degradation, and virucidal activities of TiO_2 nanoparticles, *ACS Omega*, 6 (16), 10668–10678.

[41] Almashhori, K., Ali, T.T., Saeed, A., Alwafi, R., Aly, M., and Al-Hazmi, F.E., 2020, Antibacterial and photocatalytic activities of controllable (anatase/rutile) mixed phase TiO_2 nanophotocatalysts synthesized via a microwave-assisted sol–gel method, *New J. Chem.*, 44 (2), 562–570.

[42] Aji, B.B., Shih, S.J., and Pradita, T., 2017, Controlled crystal phase of TiO_2 by spray pyrolysis method, *J. Phys.: Conf. Ser.*, 817 (1), 012021.

[43] Grey, L.H., Nie, H.Y., and Biesinger, M.C., 2024, Defining the nature of adventitious carbon and improving its merit as a charge correction reference for XPS, *Appl. Surf. Sci.*, 653, 159319.

[44] Chi, M., Sun, X., Lozano-Blanco, G., and Tatarchuk, B.J., 2021, XPS and FTIR investigations of the transient photocatalytic decomposition of surface carbon contaminants from anatase TiO_2 in UHV starved water/oxygen environments, *Appl. Surf. Sci.*, 570, 151147.

[45] Zhang, W., Li, G., Liu, H., Chen, J., Ma, S., Wen, M., Kong, J., and An, T., 2020, Photocatalytic degradation mechanism of gaseous styrene over Au/TiO_2@CNTs: Relevance of superficial state with deactivation mechanism, *Appl. Catal., B*, 272, 118969.

[46] Liu, T., Chen, W., Huang, T., Duan, G., Yang, X., and Liu, X., 2016, Titania-on-gold

nanoarchitectures for visible-light-driven hydrogen evolution from water splitting, *J. Mater. Sci.*, 51 (14), 6987–6997.

[47] Waheed, A., Shi, Q., Maeda, N., Meier, D.M., Qin, Z., Li, G., and Baiker, A., 2020, Strong activity enhancement of the photocatalytic degradation of an azo dye on Au/TiO_2 doped with FeO_x, *Catalysts*, 10 (8), 933.

[48] Zhang, K., Lu, G., Chu, F., and Huang, X., 2021, Au/TiO_2 nanobelts: Thermal enhancement vs. plasmon enhancement for visible-light-driven photocatalytic selective oxidation of amines into imines, *Catal. Sci. Technol.*, 11 (21), 7060–7071.

[49] Nasikhudin, N., Diantoro, M., Kusumaatmaja, A., and Triyana, K., 2018, Study on photocatalytic properties of TiO_2 nanoparticle in various pH condition, *J. Phys.: Conf. Ser.*, 1011 (1), 012069.

[50] Gogoi, D., Namdeo, A., Golder, A.K., and Peela, N.R., 2020, Ag-doped TiO_2 photocatalysts with effective charge transfer for highly efficient hydrogen production through water splitting, *Int. J. Hydrogen Energy*, 45 (4), 2729–2744.

[51] Din, M.I., Khalid, R., Najeeb, J., and Hussain, Z., 2021, Fundamentals and photocatalysis of methylene blue dye using various nanocatalytic assemblies-A critical review, *J. Cleaner Prod.*, 298, 126567.

[52] Somwanshi, S.B., Somvanshi, S.B., and Kharat, P.B., 2020, Visible light driven photocatalytic activity of TiO_2 nanoparticles prepared via gel-combustion process, *J. Phys.: Conf. Ser.*, 1644 (1), 012042.

[53] Toncón-Leal, C.F., Villarroel-Rocha, J., Silva, M.T.P., Braga, T.P., and Sapag, K., 2021, Characterization of mesoporous region by the scanning of the hysteresis loop in adsorption–desorption isotherms, *Adsorption*, 27 (7), 1109–1122.

[54] Zhang, M., Xu, W., Ma, C.L., Yu, J., Liu, Y.T., and Ding, B., 2022, Highly active and selective electroreduction of N_2 by the catalysis of Ga single atoms stabilized on amorphous TiO_2 nanofibers, *ACS Nano*, 16 (3), 4186–4196.

[55] Farooq, M.U., Zhang, X., Guan, Y., Chen, W., Zhou, J., Zhang, J., Qian, G., Duan, X., Zhou, X., and Yuan, W., 2023, Synergistic electronic and geometric effects of Au/CeO_2 catalyst for oxidative esterification of methacrolein, *AIChE J.*, 69 (1), e17932.

[56] Shooshtari, M., Salehi, A., and Vollebregt, S., 2021, Effect of temperature and humidity on the sensing performance of TiO_2 nanowire-based ethanol vapor sensors, *Nanotechnology*, 32 (32), 325501.

[57] Hong, T., Yin, J.Y., Nie, S.P., and Xie, M.Y., 2021, Applications of infrared spectroscopy in polysaccharide structural analysis: Progress, challenge and perspective, *Food Chem.: X*, 12, 100168.

[58] Boccuzzi, F., Chiorino, A., and Manzoli, M., 2002, Au/TiO_2 nanostructured catalyst: Pressure and temperature effects on the FTIR spectra of CO adsorbed at 90 K, *Surf. Sci.*, 502-503, 513–518.

[59] Manzoli, M., Chiorino, A., Vindigni, F., and Boccuzzi, F., 2012, Hydrogen interaction with gold nanoparticles and clusters supported on different oxides: A FTIR study, *Catal. Today*, 181 (1), 62–67.

[60] Dorranian, D., Solati, E., and Dejam, L., 2012, Photoluminescence of ZnO nanoparticles generated by laser ablation in deionized water, *Appl. Phys. A*, 109 (2), 307–314.

[61] Qutub, N., Singh, P., Sabir, S., Sagadevan, S., and Oh, W.C., 2022, Enhanced photocatalytic degradation of Acid Blue dye using CdS/TiO_2 nanocomposite, *Sci. Rep.*, 12 (1), 5759.

[62] Fathy, M., Hamad, H., and Kashyout, A.H., 2016, Influence of calcination temperatures on the formation of anatase TiO_2 nano rods with a polyol-mediated solvothermal method, *RSC Adv.*, 6 (9), 7310–7316.

[63] Huseynov, E.M., and Huseynova, E.A., 2023. Infrared spectroscopy of nanocrystalline anatase (TiO_2) particles under the neutron irradiation, *Opt. Mater.*, 144, 114351.

[64] Khorasaninejad, M., Chen, W.T., Zhu, A.Y., Oh, J., Devlin, R.C., Roques-Carmes, C., Mishra, I., and Capasso, F., 2016, Visible wavelength planar metalenses based on titanium dioxide, *IEEE J. Sel. Top. Quantum Electron.*, 23 (3), 4700216.

[65] Saha, S., Victorious, A., and Soleymani, L., 2021, Modulating the photoelectrochemical response of

titanium dioxide (TiO_2) photoelectrodes using gold (Au) nanoparticles excited at different wavelengths, *Electrochim. Acta*, 380, 138154.

[66] Rao, K.G., Ashok, C., Rao, K.V., Chakra, C.S., and Rajendar, V., 2014, Green synthesis of TiO_2 nanoparticles using hibiscus flower extract, *Proceedings of the International Conference on Emerging Technologies in Mechanical Sciences*, Telangana, India, December 26–27.

[67] Subramanian, A., Pan, Z., Li, H., Zhou, L., Li, W., Qiu, Y., Xu, Y., Hou, Y., Muzi, C., and Zhang, Y., 2017, Synergistic promotion of photoelectrochemical water splitting efficiency of TiO_2 nanorods using metal-semiconducting nanoparticles, *Appl. Surf. Sci.*, 420, 631–637.

[68] Khan, M.M., Ansari, S.A., Lee, J., and Cho, M.H., 2013, Enhanced optical, visible light catalytic and electrochemical properties of Au@TiO_2 nanocomposites, *J. Ind. Eng. Chem.*, 19 (6), 1845–1850.

[69] Kumar, A., and Pandey, G., 2017, The photocatalytic degradation of methyl green in presence of visible light with photoactive $Ni_{0.10}$:$La_{0.05}$:TiO_2 nanocomposites, *IOSR J. Appl. Chem.*, 10 (9), 31–44.

[70] Akpan, U.G., and Hameed, B.H., 2009, Parameters affecting the photocatalytic degradation of dyes using TiO_2-based photocatalysts: A review, *J. Hazard. Mater.*, 170 (2-3), 520–529.

[71] Xiao, J.D., Han, L., Luo, J., Yu, S.H., and Jiang, H.L., 2018, Integration of plasmonic effects and Schottky junctions into metal–organic framework composites: Steering charge flow for enhanced visible-light photocatalysis, *Angew. Chem., Int. Ed.*, 57 (4),1103–1107.

[72] Wang, Y.G., Cantu, D.C., Lee, M.S., Li, J., Glezakou, V.A., and Rousseau, R., 2016, CO oxidation on Au/TiO_2: Condition-dependent active sites and mechanistic pathways, *J. Am. Chem. Soc.*, 138 (33), 10467–10476.

[73] Wen, Y., Liu, B., Zeng, W., and Wang, Y., 2013, Plasmonic photocatalysis properties of Au nanoparticles precipitated anatase/rutile mixed TiO_2 nanotubes, *Nanoscale*, 5 (20), 9739–9746.

[74] Dong, S., Tebbutt, G.T., Millar, R., Grobert, N., and Maciejewska, B.M., 2023, Hierarchical porosity design enables highly recyclable and efficient Au/TiO_2 composite fibers for photodegradation of organic pollutants, *Mater. Des.*, 234, 112318.

[75] Chen, Y., Bian, J., Qi, L., Liu, E., and Fan, J., 2015, Efficient degradation of methylene blue over two-dimensional Au/TiO_2 nanosheet films with overlapped light harvesting nanostructures, *J. Nanomater.*, 2015, 905259.

[76] Jansanthea, P., and Chomkitichai, W., 2019, Enhanced photocatalytic degradation of methylene blue by using Au-TiO_2, *Appl. Mech. Mater.*, 886, 107–113.

[77] Rimal Isaac, R.S., Ashima, B., and Praseetha, P.K., 2014, Sonophotocatalytic degradation of methylene blue using synthesized M@TiO_2 nanocomposites (M= Ag, Pd, Au, Pt), *Arab J. Phys. Chem.*, 2 (4), 90–96

[78] Arias, M.C., Aguilar, C., Piza, M., Zarazua, E., Anguebes, F., and Cordova, V., 2021. Removal of the methylene blue dye (MB) with catalysts of Au-TiO_2: Kinetic and degradation pathway, *Mod. Res. Catal.*, 10 (1), 1–14.